ELSEVIER

Journal of Fluids and Structures 26 (2010) 685–702

JOURNAL OF FLUIDS AND STRUCTURES

www.elsevier.com/locate/jfs

Numerical simulation of Reynolds number effects on velocity shear flow around a circular cylinder

Shuyang Cao[a,*], Shigehira Ozono[b], Yukio Tamura[c], Yaojun Ge[a], Hironori Kikugawa[d]

[a]*State Key Lab for Disaster Reduction in Civil Engineering, Tongji University, Siping Road 1239, Shanghai 200092, China*
[b]*Faculty of Engineering, Miyazaki University, Miyazaki 889-2192, Japan*
[c]*Tokyo Polytechnic University, 1583 Iiyama, Atsugi, Kanagawa 243-0297, Japan*
[d]*Department of Mechanical Engineering, Oita National College of Technology, Oita 870-0152, Japan*

Received 25 November 2008; accepted 7 March 2010
Available online 3 April 2010

Abstract

Three-dimensional Direct Numerical Simulation (DNS) and Large Eddy Simulation (LES) are performed to investigate the shear effects on flow around a circular cylinder at Reynolds numbers of $Re = 60$–1000. The shear parameter, β, which is based on the velocity gradient, cylinder diameter and upstream mean velocity at the center plane of the cylinder, varies from 0 to 0.30. Variations of Strouhal number, drag and lift coefficients, and unsteady wake structures with shear parameter are studied, along with their dependence on Reynolds number. The presented simulation provides detailed information for the flow field around a circular cylinder in shear flow. This study shows that the Strouhal number exhibits no significant variation with shear parameter. The stagnation point moves to the high-velocity side almost linearly with shear parameter, and this result mainly influences the aerodynamic forces acting on a circular cylinder in shear flow. Both the Reynolds number and shear parameter influence the movement of the stagnation point and separation point. Mode A wake instability is suppressed into parallel vortex shedding mode at a certain shear parameter. The lift force increases with increasing shear parameter and acts from the high-velocity side to the low-velocity side. In addition, a simple method to estimate the lift force coefficient in shear flow is provided.

Keywords: Aerodynamic force; Direct numerical simulation; Large eddy simulation; Shear parameter; Vortex shedding; Wake dynamics

1. Introduction

Vortex shedding behind two-dimensional circular cylinders has been one of the most studied subjects in fluid mechanics in the past several decades because of its practical and theoretical importance. Although a quite comprehensive understanding of the vortex dynamics in a cylinder's wake has been achieved (as reflected in the reviews by Williamson (1996) and many other researchers), the simplicity of the geometry and the abundance of interesting flow features continue to make this phenomenon the subject of many current studies. The majority of past studies on

*Corresponding author. Tel./fax: +86 21 65983116x2317.
E-mail address: shuyang@tongji.edu.cn (S. Cao).

0889-9746/$ - see front matter © 2010 Elsevier Ltd. All rights reserved.
doi:10.1016/j.jfluidstructs.2010.03.003

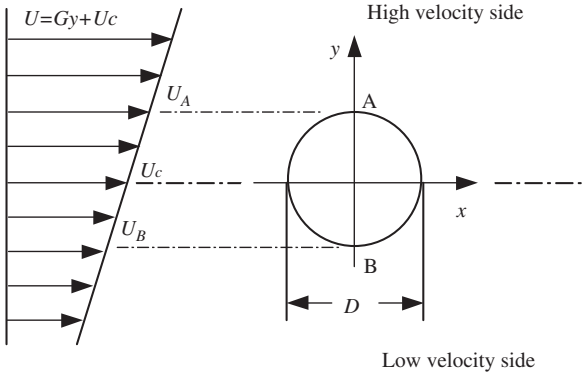

Fig. 1. Schematic of shear flow configuration.

unsteady flow past a circular cylinder were conducted under symmetric approaching flow conditions in which vortices are equivalently shed from each side of the body. However, in many practical applications, a cylindrical structure is immersed in a flow that contains some asymmetries. For example, a bridge deck is immersed in an atmospheric boundary layer with a mean velocity profile. Since strong local shear flows can be produced by special metrological phenomena, terrain effects, among others, it is important to understand the features of vortex shedding behavior and the aerodynamic forces on a circular cylinder in a shear flow. Meanwhile, identification of how the velocity shear (a simple and typical case of non-uniform approach flow) influences vortex shedding from a circular cylinder as well as wake dynamics is also a very interesting fundamental problem. The velocity difference between the high- and low-velocity sides of a cylinder increases with an increase in velocity shear. The strength and depth of the boundary layer on the two sides (and the subsequent vorticity generated in the separated shear layers) differ on the two sides. This phenomenon may create differences in vortex shedding behavior or shear layer instability on the two sides of a cylinder. This study was mainly motivated by the need to understand these behaviors. In this paper, the extent of velocity shear is expressed by the shear parameter $\beta = G(D/U_c) = (\mathrm{d}U/\mathrm{d}y)(D/U_c)$, where U_c is the mean velocity at the center plane, and D is the diameter of the circular cylinder and G is the velocity gradient, as illustrated in Fig. 1. The origin of the coordinate system is located at the center of the circular cylinder. The Reynolds number Re is based on the diameter of the cylinder D and the centerline velocity U_c. With this definition, it is easy to change the shear parameter while the Reynolds number remains unchanged.

Several experimental studies have been carried out regarding the shear effects on flow around a circular cylinder. However, there has been significant disagreement among the results, even on basic issues associated with vortex shedding behavior. Kiya et al. (1980) investigated vortex shedding from a circular cylinder in moderate Reynolds number shear flows (Re = 35–1500) in a water tank. They found that the critical Reynolds number for vortex shedding to take place is higher in shear flow than in uniform flow. They also found that the Strouhal number decreases slightly with shear parameter when the shear parameter is small and then clearly increases with shear parameter for larger shear parameters. Kwon et al. (1992) reported similar results for $0.05<\beta<0.25$ at Re = 35–1600. Adachi and Kato (1975) investigated the flow around a circular cylinder within a small variation in shear parameter ($0<\beta<0.04$) at $\mathrm{Re} = 2.67\times10^3$–$1.07\times10^4$. They reported that both the mean drag and lift force increase with shear parameter, and lift force acts from the high-velocity side to the low-velocity side. Hayashi and Yoshino (1990) investigated the aerodynamic force in one kind of shear flow ($\beta = 0.15$) at $\mathrm{Re} = 6\times10^4$ and found that drag decreases in shear flow and lift force acts from the high-velocity side to the low-velocity side. The study by Sumner and Akosile (2003) at $\mathrm{Re} = 4.0\times10^4$–$9.0\times10^4$ with a low shear parameter range of $\beta = 0.02$–0.07 showed conclusions with regard to drag and lift forces similar to those of Hayashi and Yoshino (1990), but the Strouhal number was shown to be almost unchanged with shear parameter. Fewer numerical studies exist and those that have been carried out have been restricted to two-dimensional calculations. However, these results have also been inconsistent. Tamura et al. (1980) performed a numerical study on shear flow past a circular cylinder at Re = 40 and 80 for $0<\beta<0.20$. Lei et al. (2000) carried out a two-dimensional simulation of flow at Re = 80–1000 for $0<\beta<0.25$ with an upwind difference scheme. Kang (2006) performed two-dimensional calculations at Re = 50–160 for $0<\beta<0.2$ at two kinds of blockage ratios of $B = 0.1$ and 0.05 using an immersed boundary method. The results of both Lei et al. (2000) and Kang (2006) showed that the Strouhal number remained nearly constant or slightly decreased with increasing shear rate. Both Lei et al. (2000) and Tamura et al. (1980) indicated that the front stagnation point moved to the high-velocity side in the shear

flow. However, they reported different results concerning the direction of lift force. Lei et al. (2000) found that the lift was directed towards the low-velocity side, while Tamura et al. (1980) reported that it acted in the opposite direction. Our recent experimental study (Cao et al., 2007) at $Re = 3.4 \times 10^4$ with a shear range of $0 < \beta < 0.27$ showed that the flow and aerodynamic force around a circular cylinder were influenced by the velocity shear and the movement of stagnation point simultaneously, which leads to the aerodynamic force acting in the opposite direction. As mentioned above, there are still many unknowns and further detailed study is necessary on this flow configuration.

In this study, we systematically performed three-dimensional Direct Numerical Simulation (DNS) and Large Eddy Simulation (LES) calculations to investigate the effects of velocity shear on vortex shedding from a circular cylinder and wake dynamics. From detailed flow information obtained by numerical simulation, we expect to achieve a comprehensive understanding of the mechanism of shear effects. In the numerical simulation, a co-located mesh was employed in the generalized coordinate system for finite difference approximation of the incompressible Navier–Stokes equations. The simulation was carried out for Re = 60, 80, 150, 200, 220, 500 and 1000 to investigate the Reynolds number dependence, which was one possible reason for inconsistencies in past studies. DNS was performed for Re = 60, 80, 150, 200 and 220, while LES was carried out with a dynamic Smagorinsky subgrid model for Re = 500 and 1000. A central difference scheme was applied in the simulation in order to avoid unnecessary numerical dissipation accompanying the upwind scheme. More accurate yet stable simulation can be expected from the central difference scheme, as shown by Kravchenko and Moin (2000) in their numerical studies of flow over a circular cylinder at Re = 3900. However, until now, the Reynolds number has generally been limited to 10^3 for the central difference scheme. Therefore, the Reynolds numbers considered in the present study take on values up to Re = 1000 in order to achieve more precise and stable predictions of shear effects. In this paper, the governing equations in the generalized coordinate system and corresponding numerical procedure are described first, followed by detailed validations. Then, the shear effects on Strouhal number, aerodynamic force, and the underlying physical mechanism are presented together with illustrations of the dynamic wake structure. Finally, a simple method for estimation of the lift force coefficient in shear flow is provided.

2. Problem formation and numerical details

2.1. Problem formulation

The numerical model for flow around a circular cylinder is formulated using the generalized curvilinear coordinate system. The governing equations for Direct Numerical Simulation are the continuity and Navier–Stokes equations:

$$\frac{\partial u_i}{\partial x_i} = J\frac{\partial U_m}{\partial \xi_m} = 0, \tag{1}$$

$$\frac{1}{J}\frac{\partial u_i}{\partial t} + \frac{\partial}{\partial \xi_m}(U_m u_i) = -\frac{\partial}{\partial \xi_m}\left(\frac{1}{J}\frac{\partial \xi_m}{\partial x_i}p\right) + \frac{\partial}{\partial \xi_m}\left(\nu G^{mn}\frac{\partial u_i}{\partial \xi_n}\right), \tag{2}$$

where

$$U_m = \frac{1}{J}\frac{\partial \xi_m}{\partial x_i}u_i \quad \text{and} \quad G^{mn} = \frac{1}{J}\frac{\partial \xi_m}{\partial x_i}\frac{\partial \xi_n}{\partial x_j}, \tag{3,4}$$

in which u_i ($i = 1,2,3$) are the three velocity components in a Cartesian physical space and p, t and ν denote pressure, time and kinematic viscosity, respectively. J is the Jacobian of the transformation between the physical space and computational space. U_m is the contravariant velocity component in the generalized curvilinear coordinate system and G_{mn} is the mesh skewness tensor.

Eqs. (5) and (6) show the filtered continuity and Navier–Stokes equations for large eddy simulation, in which the grid-scale turbulence is solved while the sub-grid-scale turbulence is modeled:

$$\frac{\partial \overline{u}_i}{\partial x_i} = J\frac{\partial \overline{U}_m}{\partial \xi_m} = 0, \tag{5}$$

$$\frac{1}{J}\frac{\partial \overline{u}_i}{\partial t} + \frac{\partial}{\partial \xi_m}(\overline{U}_m \overline{u}_i) = -\frac{\partial}{\partial \xi_m}\left(\frac{1}{J}\frac{\partial \xi_m}{\partial x_i}\overline{p}\right) + \nu\frac{\partial}{\partial \xi_m}\left(G^{mn}\frac{\partial \overline{u}_i}{\partial \xi_n}\right) - \frac{\partial}{\partial \xi_m}\left(\frac{1}{J}\frac{\partial \xi_m}{\partial x_j}\tau_{ij}\right), \tag{6}$$

where $\tau_{ij}=\overline{u_iu_j}-\overline{u}_i\overline{u}_j$, and all the variables are given as filtered components. The anisotropic part of the SGS stress can be expressed by

$$\tau_{ij}-\frac{\delta_{ij}}{3}\tau_{kk}=-2\nu_\tau\overline{S}_{ij}, \tag{7}$$

where $\nu_\tau=C\overline{\Delta}^2|\overline{S}|=CJ^{-2/3}|\overline{S}|$ (is the size of grid filter) and $\overline{S}_{ij}=\frac{1}{2}((\partial\xi_m/\partial x_j)(\partial\overline{u}_i/\partial\xi_m)+(\partial\xi_n/\partial x_i)(\partial\overline{u}_j/\partial x_n))$.

The following dynamic procedure based on the Smagorinsky model proposed by Germano et al. (1991) is used to determine the unknown model coefficient C:

$$L_{ij}=\widehat{\overline{u}_i\overline{u}_j}-\widetilde{\overline{u}}_i\widetilde{\overline{u}}_j,\quad M_{ij}=\overline{\Delta}^2(\alpha^2|\overline{S}|\overline{S}_i^k-|\overline{S}|\overline{S}_i^k),\quad C=-\frac{1}{2}\frac{\langle L_{ij}M_{ij}\rangle_z}{\langle M_{ij}M_{ij}\rangle_z},$$

where the tilde means the operation of a test filter. The scale ratio of the test filter to grid filter is the only parameter in the procedure and is assigned the value of 2.0, as suggested by Germano et al. (1991). Averaging and a test filter operation are performed only in the homogeneous spanwise direction, in conjunction with Lilly's least-squares technique (1992). To avoid numerical instability, the negative value of the SGS eddy viscosity is truncated to zero. Large Eddy Simulation using the dynamic Smagorinsky model has been widely utilized as a relatively affordable and easy-to-use approach for simulation of separated flow and other complicated flows (Kravchenko and Moin, 2000).

2.2. Numerical discretization and algorithm

We utilized the non-staggered-grid method developed by Zang et al. (1994) for solving three-dimensional, time-dependent incompressible Navier–Stokes equations for unsteady calculations in curvilinear coordinates. In the computational space, the Cartesian velocity components and the pressure are defined at the center of a control volume, while the volume fluxes are defined at the midpoint of their corresponding cell surface. Fourth-order central difference and fourth-order interpolation are used for the convection terms, while a second-order central difference scheme is used for the diffusion terms. The continuity equation is discretized at the point where pressure is defined using contravariant velocity components. For time marching, the explicit Adams–Bashforth differencing scheme is applied for the convention term, and the semi-explicit Crank–Nicolson formulation is applied for the diffusion term. The numerical procedure is based on the fractional step method, which is briefly described below.

First, the intermediate Cartesian velocity components u_i^* can be calculated according to

$$u_i^*=u_i^n+\Delta t\times J\left(\frac{3}{2}C_i^n-\frac{1}{2}C_i^{n-1}+\frac{1}{2}\nu\frac{\partial}{\partial\xi_m}\left(G^{mn}\frac{\partial(u_i^*+u_i^n)}{\partial\xi_n}\right)\right), \tag{8}$$

where $C_i^n=-(\partial/\partial\xi_m)(U_mu_i)^n$ for DNS or $C_i^n=-(\partial/\partial\xi_m)(U_mu_i)^n-(\partial/\partial\xi_m)((1/J)(\partial\xi_m/\partial x_j)\tau_{ij})^n$ for LES. By conducting a coordinate transform on u_i^*, the contravariant velocity components at the cell center can be obtained and can be interpolated to contravariant velocity components U_m^* defined at the cell surface.

Then, the potential field of the next step can be computed iteratively by solving the Poisson equation, Eq. (9), using the successive over-relaxation (SOR) method:

$$\frac{\partial}{\partial\xi_m}\left(G^{mn}\frac{\partial\phi^{n+1}}{\partial\xi_n}\right)=\frac{1}{\Delta t}\frac{\partial U_m^*}{\partial\xi_m}), \tag{9}$$

$$u_i^{n+1}=u_i^*-\Delta t\frac{\partial\xi_m}{\partial x_i}\frac{\partial\phi^{n+1}}{\partial\xi_m}, \tag{10}$$

$$U_m^{n+1}=U_m^*-\Delta t\left(G^{mn}\frac{\partial\phi^{n+1}}{\partial\xi_n}\right). \tag{11}$$

Finally, the contravariant and Cartesian velocity components of the next step can be calculated from Eqs. (10) and (11), respectively. This algorithm has been utilized in many numerical simulations.

2.3. Numerical model and boundary conditions

To adequately resolve the flow, an O-type body-fitted grid system is used. The computational domain is basically $30D$ on the circular plane by $4D$ in the spanwise direction for all Reynolds numbers, but the spanwise domain is $8D$ for Re = 200 and

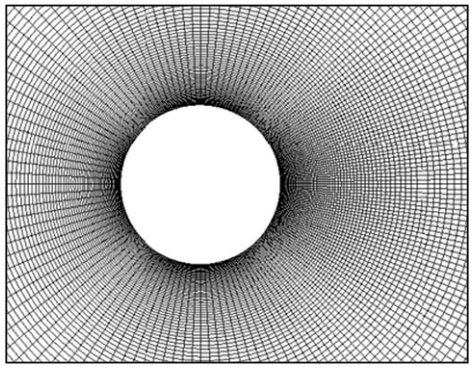

Fig. 2. Grid example near cylinder.

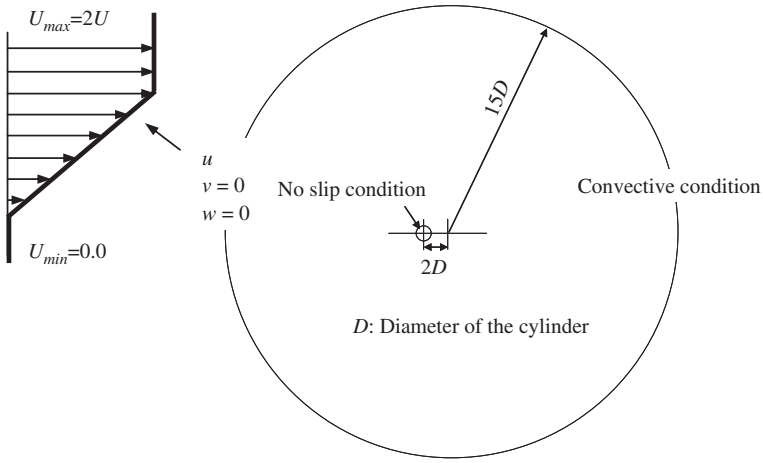

Fig. 3. Computational domain and boundary conditions.

220. The vortex instability experiences mode change in the Reynolds number range of $50<\mathrm{Re}<1000$, and one feature of transient mode A instability is an approximately $4D$ wavelength structure in the spanwise direction. Therefore, the computational domain in the spanwise direction is set to $8D$ for $\mathrm{Re}=200$ and 220 in order to illustrate mode A wake dynamics more clearly. The grid number on the circular plane is 160×140 for all Reynolds numbers, while it is set to 40 or 80 in the spanwise direction, depending on whether the computational domain is $4D$ or $8D$. For more efficient simulations, the computational domain is spatially resolved such that a dense clustering of grid points is applied near the cylinder, especially in the wake zone, while a coarser grid is used away from the cylinder. The grid size stretches outwards to the boundary with a tangential-hyperbolic grid distribution, with the first grid near the body surface and the last grid near the outer boundary of computational domain given explicitly as $0.1/\sqrt{\mathrm{Re}}$ and 0.5, respectively. Fig. 2 illustrates an example of a grid near the cylinder. Fig. 3 shows the computational domain and boundary conditions.

The boundary conditions for simulation are as follows:

Cylinder body surface: A no-slip condition for velocity u_i and a Neumann condition for pseudo-pressure ϕ are imposed.

Inlet: A Dirichlet boundary condition of velocity, i.e., $U=1+Gy$, $v=0$ and $w=0$, and a Neumann condition of pseudo-pressure ϕ are imposed at the inlet boundary. In order to avoid the reversed flow at the inlet, U is truncated to zero when it is negative if $y<-1/G$. Therefore, it is not a perfect case of homogeneous shear flow at the inlet. At the strongest shear case of $\beta=0.3$, the length at which the velocity shear at the inlet is maintained as constant is about $7D$. This may influence the flow inside the computational domain in a way similar to a blockage effect.

Outflow boundary: A convective boundary condition of the form $(\partial/\partial t)+c(\partial/\partial x)=0$ is applied for both velocity and pseudo-pressure. In order to ensure global mass conservation, c is taken to be the bulk velocity.

Spanwise: A periodic condition for velocity and pseudo-pressure is applied.

In addition, proper boundary conditions are imposed for the intermediate (split) velocity field, $u_i^*=u_i^{n+1}+\Delta t(\partial\phi^n/\partial x_i)$, as proposed by Kim and Moin (1985) to guarantee the precision of discretization.

2.4. Numerical validation

Detailed comparison of the first- and second-order turbulence statistics on the near and far wakes is ideal for the validation. However, there are no reliable experimental data available in this Reynolds number range. Therefore, in this study, the numerical model is validated by first comparing the Reynolds number dependence of the Strouhal number

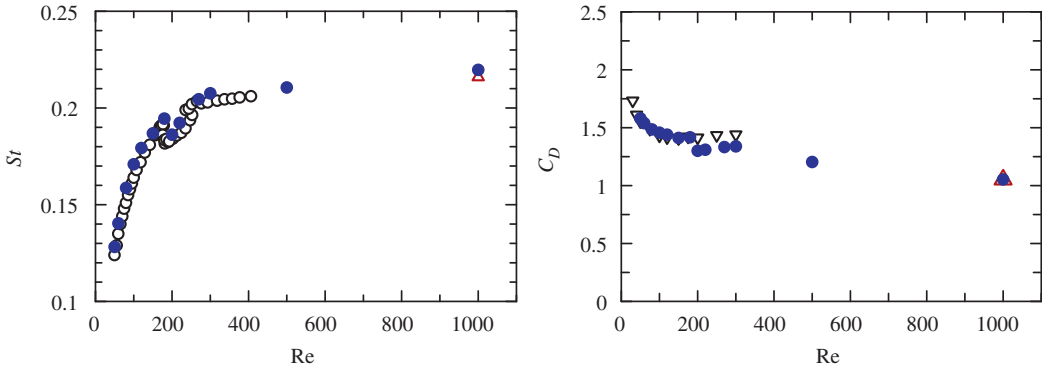

Fig. 4. Reynolds number dependence of Strouhal number and drag coefficient: ●, present cal.; ○, experiments of Williamson (1996); △, LES of Tamura and Kitagishi (2001) and ▽, DNS of Zhang et al. (1995).

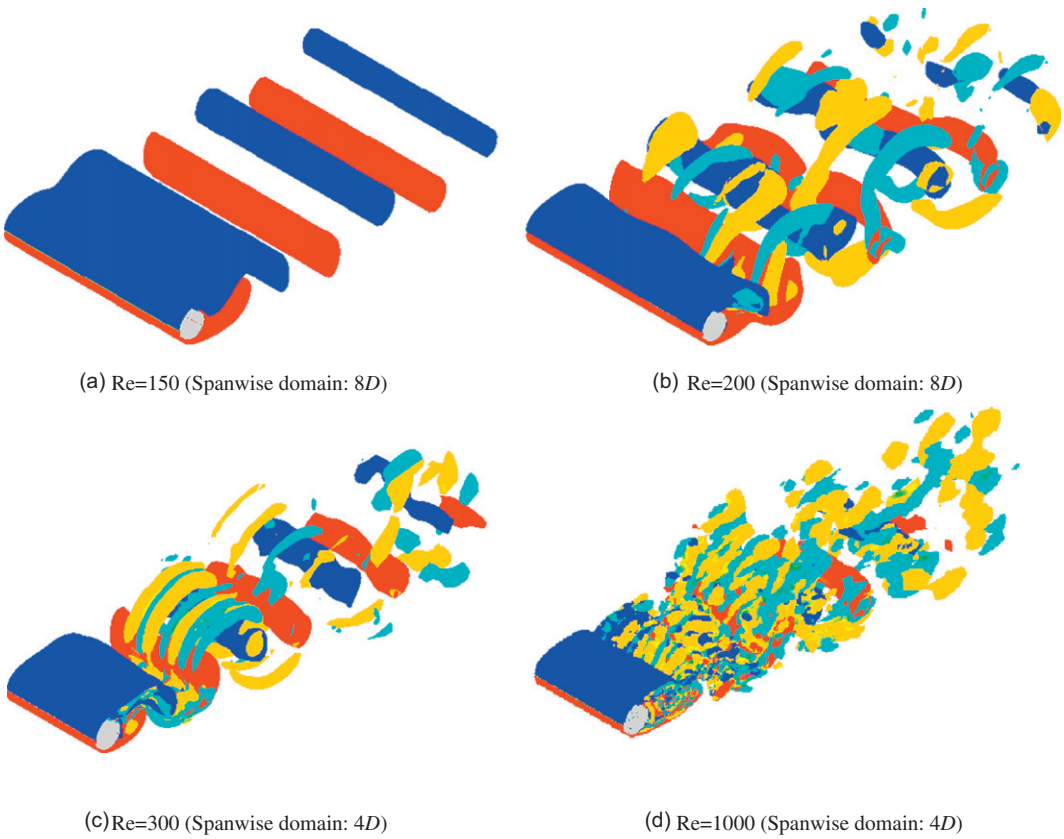

Fig. 5. Isovorticity surface of instantaneous dynamic wake at Re = 150, 200, 300 and 1000 ($|\omega_z| = 1.0$, $|\omega_x| = 0.6$. The spanwise domain is $8D$ for Re = 150 and 200, but $4D$ for Re = 300 and 1000).

and drag coefficient of a circular cylinder on Reynolds number in the range of Re = 50–1000, and then comparing the turbulence statistics and instantaneous turbulent structure at Re = 1000 with those of Kravchenko and Moin (2000) at Re = 3900. Fig. 4 compares the present results for Strouhal number and drag coefficient with those of Williamson (1996) and others. Agreements between the tendencies of the variations of St and C_D with Reynolds number for the present study and other studies are recognized. The Reynolds number range of Re = 50–1000 exhibits a change of vortex dynamics from parallel laminar shedding (Re < 180–190) to mode A (Re˜190–260) and then mode B (Re > 260) vortex shedding (Williamson, 1996). The discontinuity in the St–Re curve due to the wake transition is reproduced in the present simulation. Fig. 5 illustrates the iso-vorticity surface of the instantaneous flow field at Re = 150, 200, 300 and 1000. At Re = 150 (Fig. 5(a)), the wake presents strong two-dimensionalities due to the parallel laminar shedding mode. At Re = 200 (Fig. 5(b)) within a transient Reynolds number regime, streamwise vorticity in the formation of a braid between Karman vortices can be noticed. The spanwise wavelength obtained is about 4*D*, which can be observed more clearly in Fig. 9(a). At Re = 300, the spanwise wavelength obtained is about 1*D*, corresponding to mode B wake instability. The spanwise structure of streamwise vortices becomes more delicate at Re = 1000 (Fig. 5(d)). The three-dimensionalities of the dynamic wake structure are reproduced in the present simulation.

The Large Eddy Simulation results are further validated by comparing the mean, fluctuating and instantaneous flow structures. Fig. 6 compares the turbulence statistics obtained at Re = 1000 by the present LES with those of Kravchenko and Moin (2000) at Re = 3900, as well as the experimental results of Lourenco and Shih (1993) and Ong and Wallace (1996) at the same Reynolds numbers that were used by Kravchenko and Moin (2000) for comparison purposes. The Strouhal number and aerodynamic forces at Re = 1000 and 3000 do not differ from each other significantly, and therefore the comparison of turbulent statistics between these two Reynolds numbers may show the overall accuracy of present simulation. Fig. 6 shows that present study provides reasonably good simulation results. The streamwise mean velocity obtained in the present simulation agrees with the experimental results better than those of Kravchenko and Moin (2000), especially in the near wake, although the velocity fluctuation fluctuates somewhat more from the experimental data. Fig. 7 compares the instantaneous separating shear layers and development of

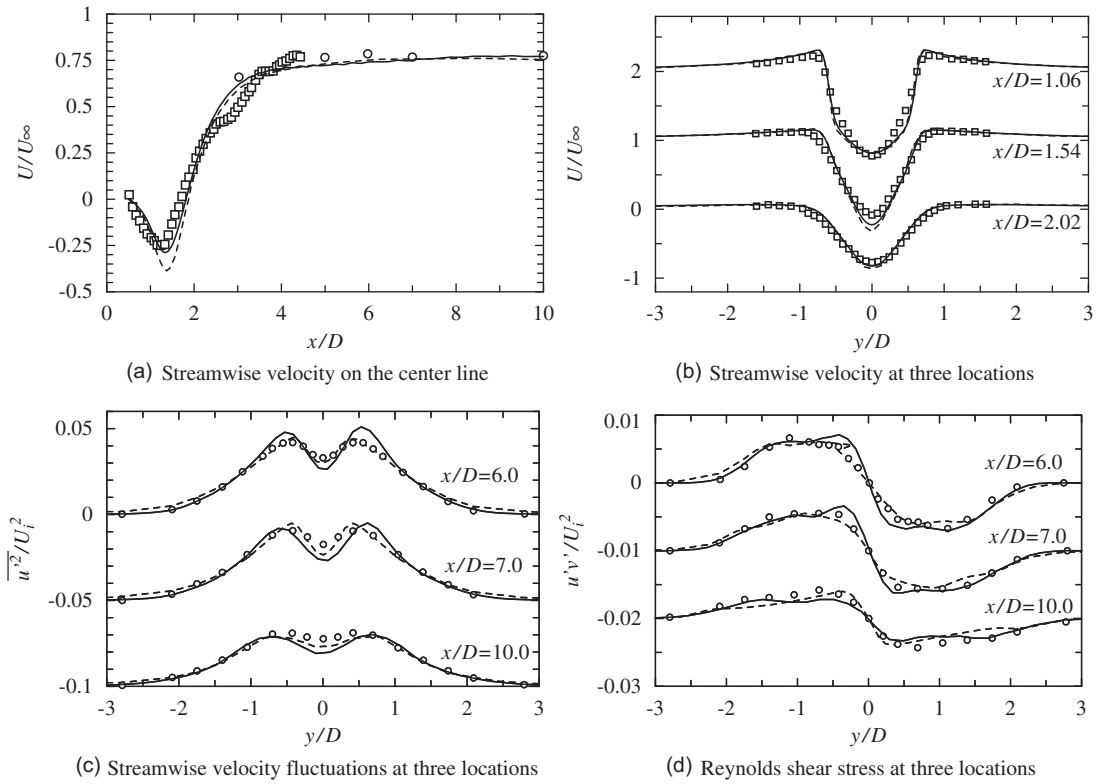

Fig. 6. Comparison of the turbulence statistics in the wake of a circular cylinder: —, Present LES at Re = 1000; - - -, LES at Re = 3900 of Kravchenko and Moin; □, experiment of Ong and Wallace; ○, experiment of Lourenco and Shih.

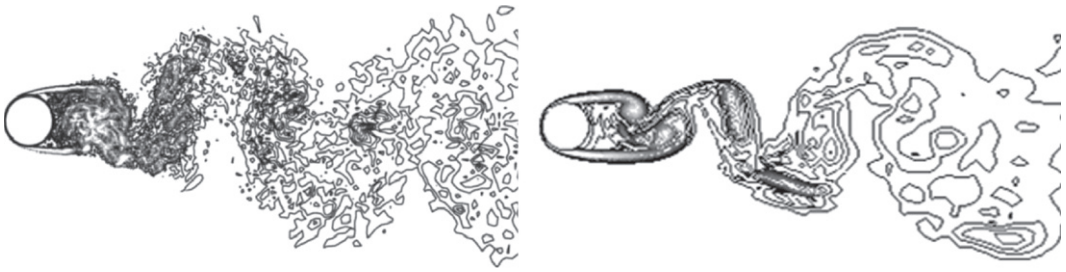

(a) LES at Re=3900 of Kravchenko and Moin; (b) Present study

Fig. 7. Comparison of separating shear layers and development of Karman vortex street. Shown are 16 contours of instantaneous vorticity magnitude from $\omega = 0.5$ to 10.

Table 1
Grid independence study.

	Re	Domain	Grid number	S_t	C_D	C_L
Present (DNS)	200	x–y plan: $30D$ z dir.: $8D$	$160 \times 140 \times 80$ $128 \times 112 \times 64$ $102 \times 90 \times 51$	0.186 0.186 0.189	1.300 1.298 1.312	0.370 0.379 0.393
Williamson (1996)	200	Experiment		0.184		
Present (LES)	1000	x–y plan: $30D$ z dir.: $4D$	$160 \times 140 \times 40$ $128 \times 112 \times 32$ $102 \times 90 \times 26$	0.217 0.217 0.219	1.095 1.103 1.157	0.177 0.170 0.262
Tamura and Kitagishi (2001) (LES)	1000	x dir.: $29D$ y dir.: $18D$ z dir.: $4D$	$201 \times 281 \times 101$	0.216	1.020	0.080
Cantwell and Coles (1983)	1000	Experiment		0.19–0.22	1.0	

Karman vortex street in the flow. The turbulent structure obtained by Kravchenko and Moin (2000) is much finer than that of the present study, especially in the far wake. The use of comparatively sparser grids in the present study is one reason for this, in addition to the difference in Reynolds number.

Grid independence is checked at $\mathrm{Re} = 200$ (DNS) and 1000 (LES) and the results are summarized in Table 1. In general, both the Strouhal number and the drag coefficient obtained converge well with respect to the spatial resolution. In addition, 3-D wake structures can be clarified in all three grid systems.

3. Numerical results and discussion

3.1. Vortex shedding in shear flow

Fig. 8(a) shows the variation of Strouhal number, S_t, with shear parameter at $\mathrm{Re} = 60$, 150, 200, 220, 500 and 1000. Strouhal number is defined as $S_t = f \times D/U_c$, where vortex shedding frequency f is detected by FFT from the aerodynamic force on the cylinder. As seen in Fig. 8(a), the Strouhal number shows a very small decrease or increase with shear parameter at all Reynolds numbers even though its magnitude varies due to Reynolds number dependence. The variation of Strouhal number is so small that the Strouhal number can be considered unchanged with shear parameter at these Reynolds numbers. The observations of Strouhal number from past studies are shown in Fig. 8(b) for comparison. The results of the present study agree with those of the experimental studies of Sumner and Akosile (2003) and our group (Cao et al., 2007) at higher Reynolds number, and show little difference from the numerical results of Lei et al. (2000) and Kang (2006). Lei et al. (2000)

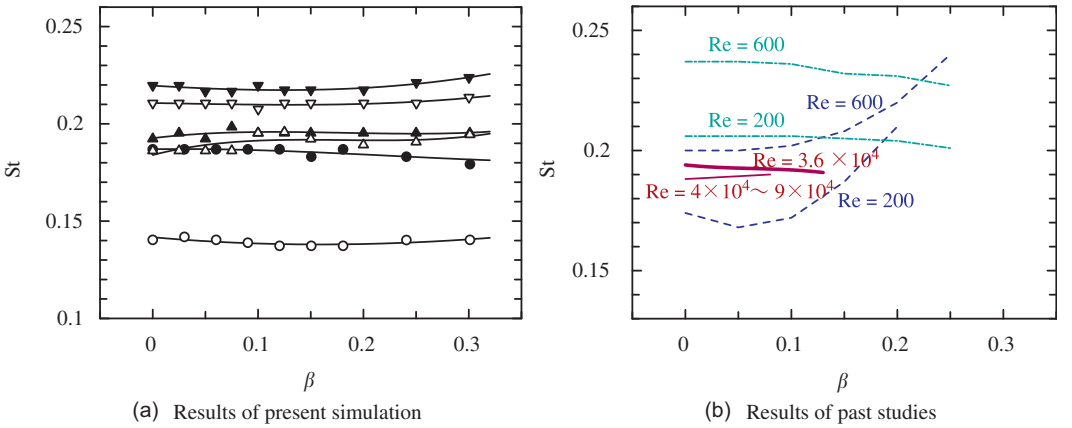

Fig. 8. Variation of Strouhal number with shear parameter. In (a): ○, Re = 60; ●, Re = 150; △, Re = 200; ▲, Re = 220; ▽, Re = 500; ▼, Re = 1000. In (b): ----, Kiya et al. (1980), - · - ·, Lei et al. (2000); ▬, Cao et al. (2007) and ——, Sumner and Akosile (2003).

showed that the Strouhal number decreased, and Kang (2006) showed that it remained nearly constant or slightly decreased with increasing shear rate. The two-dimensional simulation carried out by both of these studies is a possible reason for this difference. However, our present results clearly contradict the results of Kiya et al. (1980) and Kwon et al. (1992). In their experimental study, Kiya et al. (1980) found that vortex shedding disappeared for sufficiently large shear parameters (for instance, the case of $\beta = 0.15$ at Re = 79) and the critical Reynolds number above which vortex shedding occurs depends on shear parameter. Meanwhile, they observed an obvious increase of Strouhal number with increasing shear parameter, as shown in Fig. 8(b). The present results show that vortex shedding never disappears, even under very large shear parameters at low Reynolds number. As shown later, the vortex may disappear in the far wake at the low velocity side, but it still exists at the near wake. The phenomenon of Karman vortex shedding becoming completely suppressed in shear flow never occurred in the 2-D numerical simulations of Lei et al. (2000) and Kang (2006) and the numerical work of Kiya's group (Kiya et al., 1980). It seemed to the authors that there was some kind of mismatch between the numerical and experimental studies on the shear flow over a circular cylinder.

However, we observe some evidence of suppression of three-dimensionality by velocity shear in the transient Reynolds number regime. Fig. 9 compares the iso-vorticity surface of the instantaneous near-wake structure at $\beta = 0$ (non-shear flow), $\beta = 0.05$, 0.1 and 0.2 at Re = 200. Fig. 9(a) shows that the wavelength of the streamwise vortex is about $4.0D$ under the non-shear flow condition. With an increase in shear parameter, for instance at $\beta = 0.05$, the braid between Karman vortices becomes simpler in structure. The variation of three-dimensionality in the spanwise direction of both the primary Karman vortices and streamwise vortices becomes very unitary, i.e., only the $4D$ wavelength pattern in the spanwise structure can be observed, with almost all other wavelength components suppressed (Fig. 9(b)). The wake structure changes to the two-dimensional parallel vortex shedding mode at $\beta = 0.1$ (Fig. 9(c)). This means that the three-dimensional transition is suppressed by the shear parameter. With further increase in shear parameter, for instance at $\beta = 0.2$, the variation of Karman vortex in the spanwise direction is suppressed (Fig. 9(d)) in a similar manner to that at $\beta = 0.1$, but a kind of regular streamwise vortex structure is observed in the spanwise direction. The same phenomenon is observed at Re = 220, which suggests that the suppression of three-dimensionality by velocity shear from Mode A to parallel shedding is an inherent phenomenon. In addition, simulation with a finer grid ($196 \times 160 \times 120$) is performed for the shear effects at Re = 200 and the same phenomenon is observed. We hypothesize that the coherent 3-D structures in the oncoming shear flow contribute to this phenomenon. As indicated by Williamson (1996), the modes of 3-D shedding in wake transition have some analogy with the streamwise vortex structures found in free mixing shear layers. On the other hand, Kida and Tanaka (1994) have shown that the 3-D structures in free homogenous shear layers are analogous with those in boundary layer shear flow, where the 3-D coherent structures of the longitudinal vortex vary with Reynolds number, surface condition and other parameters. We may suggest that this potential 3-D structure of the longitudinal vortex in oncoming shear flow leads to the suppression of three-dimensionality during the interaction with the vortex shedding. Although the suppression of three-dimensionality has not yet been supported by experiments, it is worth mention here because it is found for the first time (to the author's knowledge), although it is not the main purpose of the present study. The obvious change of Strouhal number around $\beta = 0.1$ for Re = 200 and 220 in Fig. 8(a) is caused by this mode change, just as the discontinuity in the St–Re curve (Williamson, 1996) is caused by wake transition. In contrast, we did not observe the phenomenon of suppression of three dimensionality at Re = 1000 (Figs. 10(a)–(d)).

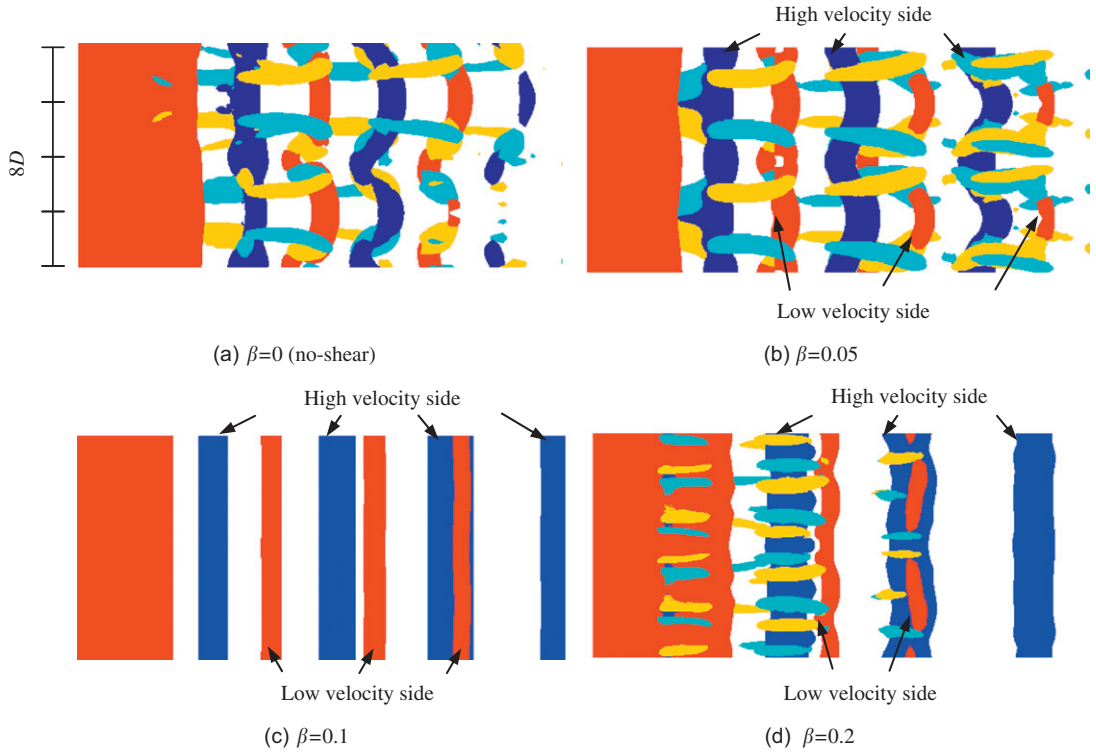

Fig. 9. Variation of iso-vorticity surface of instantaneous wake structure with shear parameter at Re = 200 ($|\omega_z| = 1.0$, $|\omega_x| = 0.6$).

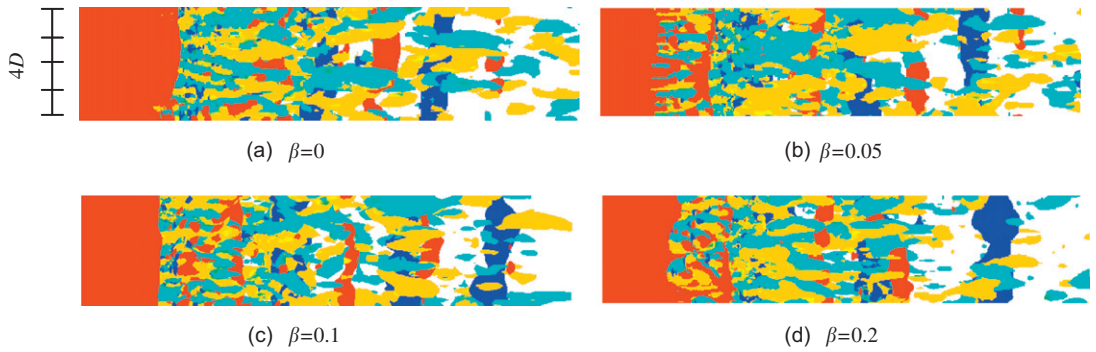

Fig. 10. Variation of iso-vorticity surface of instantaneous wake structure with shear parameter at Re = 1000 ($|\omega_z| = 1.0$,$|\omega_x| = 0.6$).

Although it can be observed from Figs. 9 and 10 that the vortex formation is different on the two sides of the cylinder, Fig. 11 presents the shear effects on the wake dynamics more clearly by illustrating the behavior of the primary Karman vortex at Re = 150 and 1000. The positive and negative vortices do not appear alternatively or regularly in shear flow. The distance between Karman vortices on the high-velocity side is different from that on the low-velocity side in the wake due to the different advection velocities on the two sides. Figs. 11(e) and (f) show that the vortices on the low-velocity side even disappear at the far wake under the strong shear condition. Fig. 12 compares the distribution of spanwise-averaged streamwise velocity fluctuation and Reynolds stress ($\overline{u'v'}$ component) for several shear parameters ($\beta = 0$, 0.1, 0.2 and 0.3) at several downstream locations ($x/D = 1.0$, 3.0, 5.0 and 9.0). Both streamwise turbulence fluctuation and Reynolds stress change with shear parameter and Reynolds number in a very complicated manner at the wake. The tendency of this change can be clarified at the near wake only. Their values at the low-velocity side are generally greater than those on the high-velocity side at the near wake, for instance at $x/D = 3.0$, and they increase with

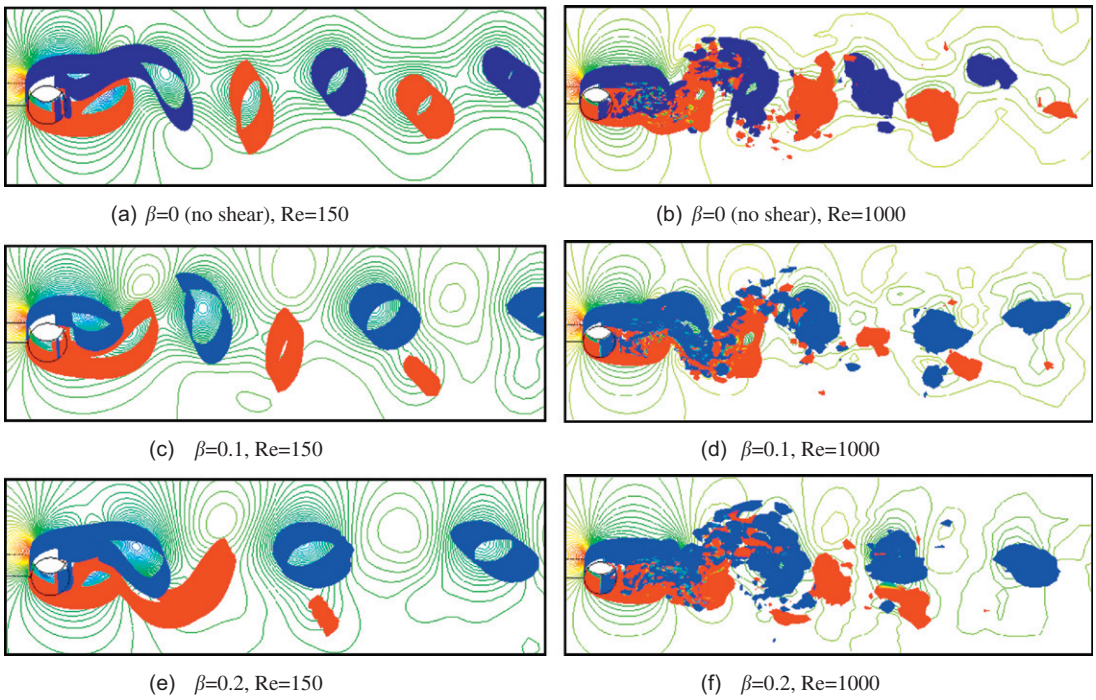

Fig. 11. Iso-vorticity (ω_z) surface of instantaneous wake structure influenced by velocity shear (background: pressure contour).

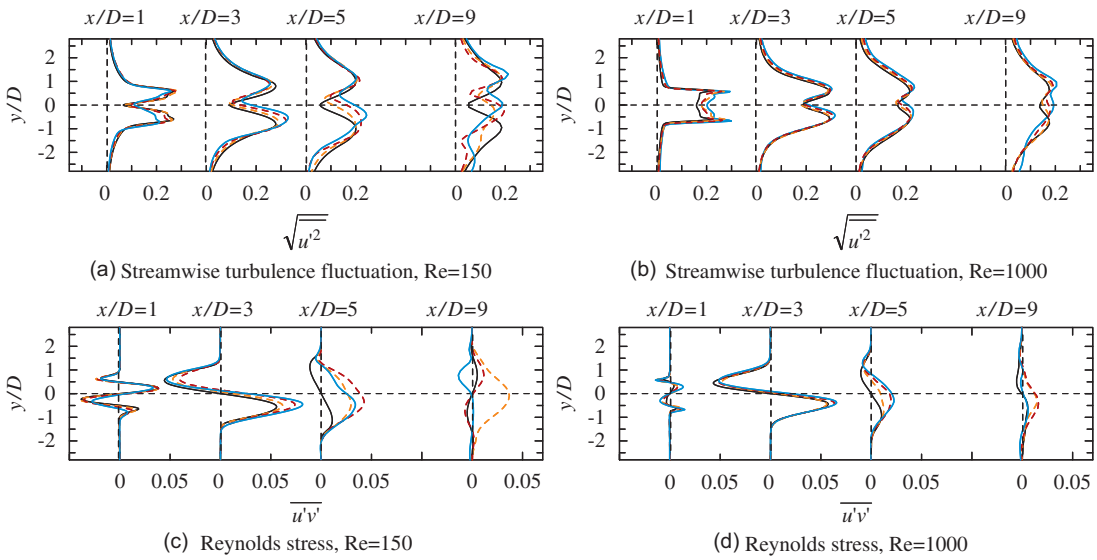

Fig. 12. Distribution of turbulence statistics in the wake of a circular in shear flows: —, $\beta=0$; - - -, $\beta=0.1$; - - -, $\beta=0.2$; ——, $\beta=0.3$.

increase in shear parameter. The locations of peak values of turbulence fluctuation move to the high-velocity side. The very complicated distribution of Reynolds stress in the far wake implies complicated unstable formation of Karman vortex. The complicated turbulence structures in the wake are very important when considering the environmental disturbance downstream of a large structure.

As observed in our previous experimental work (Cao et al., 2007), the movements of the stagnation point and separation points are significant phenomena for flow around a circular cylinder under the influence of velocity shear.

The movement of the stagnation point with shear parameter at all investigated Reynolds numbers is shown in Fig. 13, where θ_0 is the flow stagnation point angle. The flow stagnation point in the shear flows is not at $\theta_0 = 0$ as in the non-shear flow. Fig. 13 shows that the stagnation points move to the high-velocity side in shear flow, and the stagnation point angle increases almost linearly with shear parameter for all Reynolds numbers. The Reynolds number dependence of the movement of the stagnation point is shown in Fig. 14. At low Reynolds numbers, the stagnation point angle decreases with increasing Reynolds number for a given shear parameter but becomes almost constant when the Reynolds number is larger than Re = 500. This suggests that the Reynolds number effect on the movement of the stagnation point is small at much higher Reynolds numbers.

Figs. 15(a) and (b) show the variation of separation points with shear parameter on the high- and low-velocity sides individually. θ_H and θ_L are the angles of the separation point on the two sides. The separation point moves downstream on the high-velocity side and upstream on the low-velocity side, almost linearly with shear parameter. Fig. 16 presents the variation of separation points on the high- and low-velocity sides with Reynolds number. As in the non-shear condition, the separation points on both the high- and low-velocity sides move upstream almost linearly with the logarithm of Reynolds number at Re = 60–1000. The Reynolds number greatly influences the movements of separation point. In addition, the separation point at Re = 300 for non-shear flow is 106.6 in the present simulation, which agrees closely with the corresponding angle of 106.5° obtained by Persillon and Braza (1998).

The flow field around the circular cylinder changes with the movements of the stagnation point and separation points. Fig. 17 compares the mean velocity profiles around a circular cylinder at Re = 1000 and $\beta = 0.2$ at several streamwise locations between non-shear or shear-flow conditions. In the uniform flow condition, the flow accelerates symmetrically on both sides of the circular cylinder. In the shear flow condition, it can be observed that the flow on the low-velocity side accelerates greatly compared to that on the high-velocity side at all streamline locations. The differences in velocity

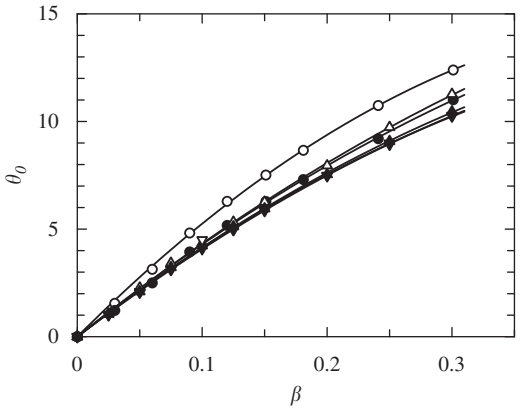

Fig. 13. Movement of stagnation point with shear parameter: ○, Re = 60; ●, Re = 150; △, Re = 200; ▲, Re = 220; ▽, Re = 500 and ▼, Re = 1000.

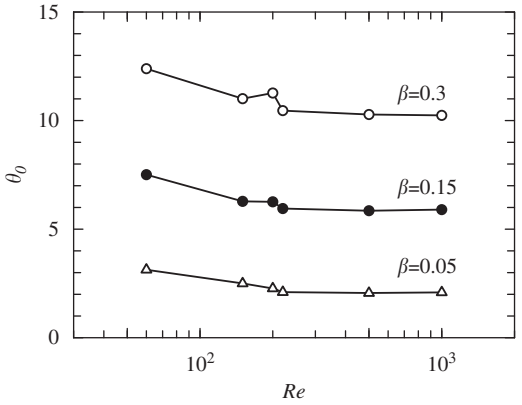

Fig. 14. Dependence of movement of stagnation point with Reynolds number.

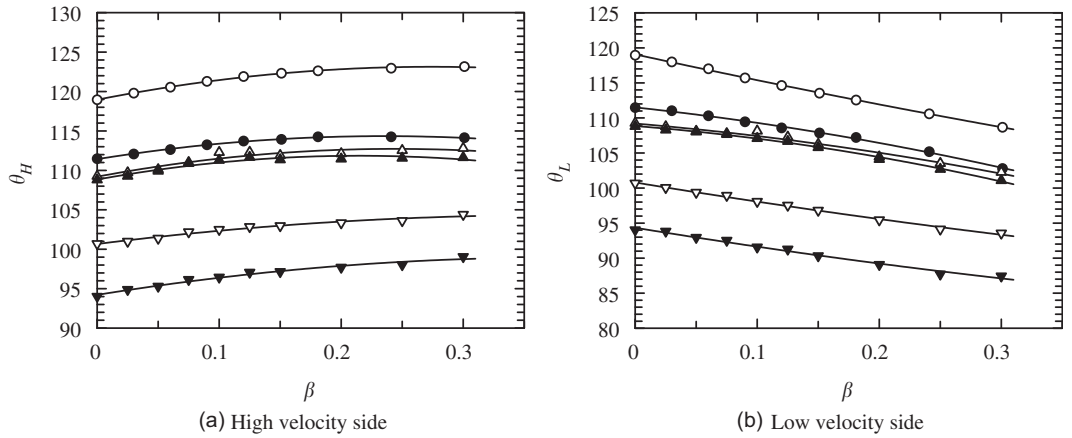

Fig. 15. Variation of separation point with shear parameter: ○, Re = 60; ●, Re = 150; △, Re = 200; ▲, Re = 220; ▽, Re = 500; ▼, Re = 1000.

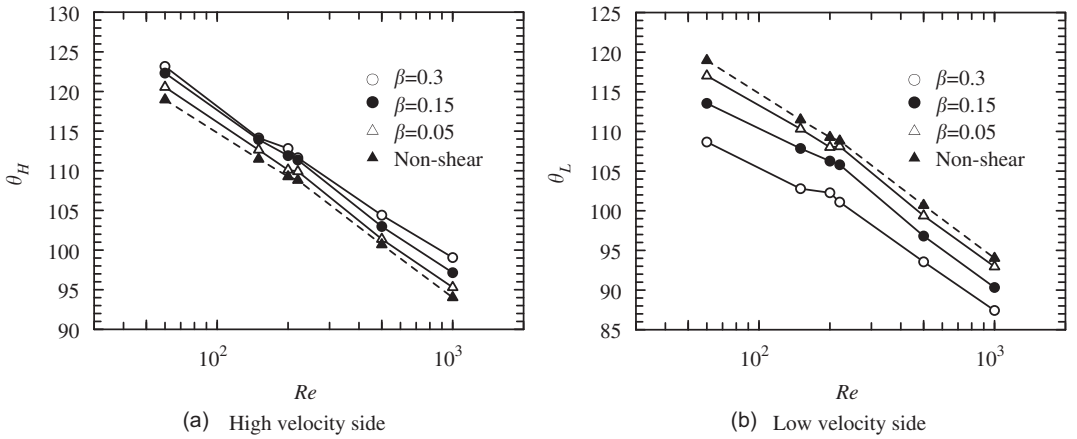

Fig. 16. Variation of separation point with Reynolds number.

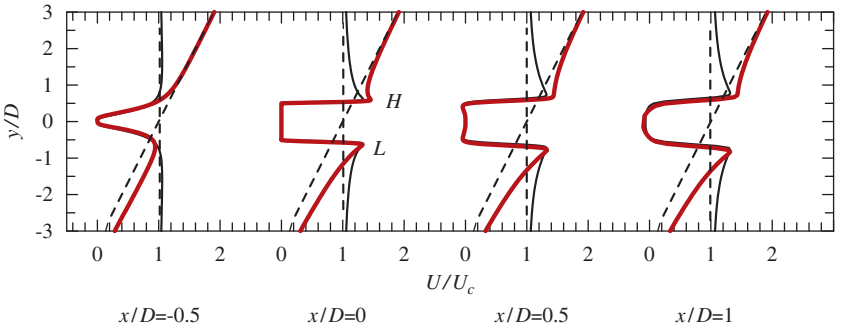

Fig. 17. Mean velocity field around the cylinder (Re = 1000, β = 0.2): - - -, oncoming flow; —, wake in non-shear flow and ▬, wake in shear flow.

that the cylinder experiences are not as strong as in the oncoming flow. In other words, the asymmetry in the oncoming velocity profile is 'self-adjusted' to some extent by the cylinder itself. In our experimental study (Cao et al., 2007), it was noticed that the vortex shedding frequencies were the same on the two sides of the cylinder at location $x/D=1.0$. The acceleration was also noticed on the low-velocity side in the wake, but it was impossible to closely measure the model to

investigate the velocity field in the boundary layer near the separation point in the experiment. How the velocity difference between the high- and low-velocity sides varies with the shear parameter at the location of $x/D = 0$ (center of the cylinder) is of interest to us. The location of maximum velocity in the velocity profile, such as points H and L in Fig. 17, generally corresponds to the location of the separated layer. Thus, the variations between the velocity differences at these two points, $\Delta U/U_c = (U_H - U_L)/U_C$, with shear parameter and Reynolds number have important implications in understanding the flow mechanism. Fig. 18 shows the variation of $\Delta U/U_c$ with shear parameter at $x/D = 0$ as illustrated by solid lines. The value of $\Delta U/U_c$ at large shear parameters for Re = 60 is not shown because it is not possible to identify the point of U_H in the velocity profile. Meanwhile, the velocity difference in the oncoming flow between the top and bottom of the cylinder is shown by a broken line for comparison. The magnitude of the shear parameter equals the velocity difference, i.e., $\beta = 0.2$ means $\Delta U/U_c = (U_A - U_B)/U_C = 0.2$ (refer to Fig. 1) in the oncoming flow. Fig. 18 shows that the velocity difference experienced by the cylinder increases almost linearly with shear parameter for all Reynolds numbers and is about 55% of that in the oncoming flow, except for Re = 60. However, the velocity difference does not disappear. The strength and depth of the boundary layer, and then the vorticity generated in the separated shear layers, still differ on the two sides. It can also be observed from Fig. 18 that, for a given shear parameter, the velocity difference decreases with Reynolds number at low Reynolds numbers and remains almost unchanged when the Reynolds number is greater than Re = 500. It seems appropriate to assume that the velocity difference and then the unbalanced separated shear layer still exist at much higher Reynolds numbers.

3.2. Aerodynamic forces

Fig. 19(a) compares the pressure distributions around a cylinder in non-shear and shear flows at Re = 1000. $\theta = 0$ is the stagnation point on the fore-body for the non-shear flow. The pressure coefficient C_p is defined as $C_p = (P - P_\infty)/(0.5\rho U_c^2)$, where P is the local mean pressure on the cylinder surface, P_∞ is the pressure upstream of the cylinder and ρ is the density of the fluid. Fig. 19(a) shows that the pressure distribution around a circular cylinder is asymmetric in the shear flows, and movement of the stagnation point to the high-velocity side is observed. The pressure coefficient is larger on the high-velocity side from the stagnation point to the point where the pressure is minimum (hereafter referred to as zone A, as shown in Fig. 19(b)), while it is larger on the low-velocity side from the minimum pressure point to the separation point (hereafter referred to as zone B). The difference between the pressure coefficients on the high- and low-velocity sides increases with increasing shear parameter. There is no significant difference between the pressure coefficients on the two sides of the cylinder in the afterbody (hereafter referred to as zone C) because it is determined by interaction of the two separated shear layers. Fig. 19(a) shows that the separation point in the shear flow moves downstream on the high-velocity side and moves upstream on the low-velocity side, and the movements of the separation point are more significant with increase in shear parameter. The pressure distribution in zone A is mainly caused by the movement of the stagnation point, while that in zone B is mainly caused by the movement of separation points, which is a direct result of the difference between the velocities on the two sides of the cylinder. This means that the pressure distribution around the circular cylinder receives the combined effects of velocity shear and accompanying movement of the stagnation point. The variations of pressure distribution at other Reynolds numbers are not shown

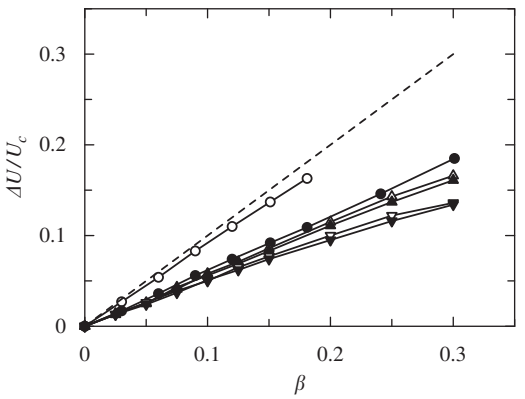

Fig. 18. Variation of mean velocity difference with shear parameter at $x/D = 0$: ○, Re = 60; ●, Re = 150; △, Re = 200; ▲, Re = 220; ▽, Re = 500 and ▼, Re = 1000.

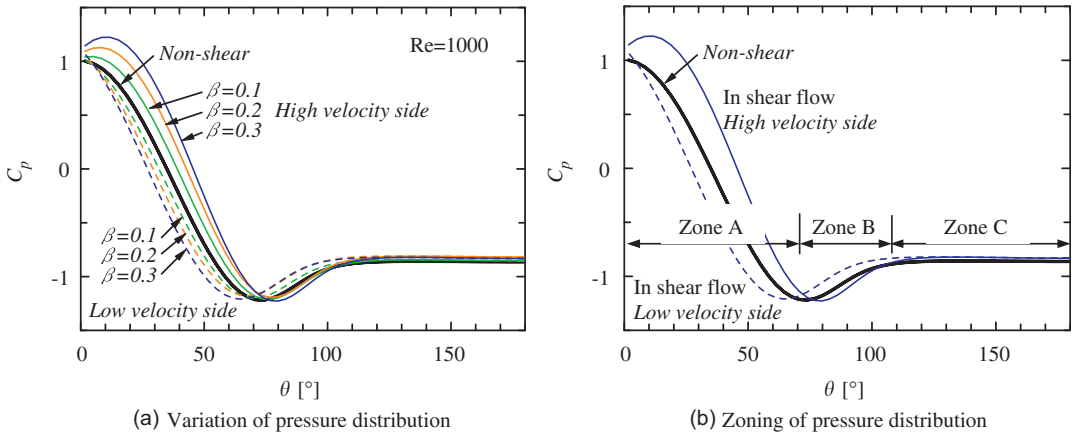

(a) Variation of pressure distribution (b) Zoning of pressure distribution

Fig. 19. Variation of pressure distribution with shear parameter and its zoning.

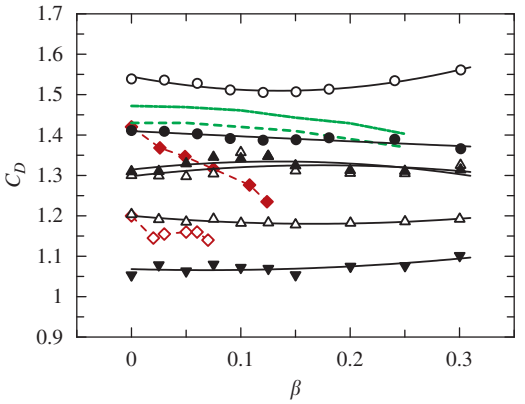

Fig. 20. Variation of drag coefficient with shear parameter at different Reynolds numbers: ○, Re = 60; ●, Re = 150; △, Re = 200; ▲, Re = 220; ▽, Re = 500; ▼, Re = 1000; ◇, Sumner and Akosile (2003); ◆, Cao et al. (2007); – –, Re = 200, Lei et al. (2000) and ·····, Re = 600, Lei et al. (2000).

here because they are very similar to that at Re = 1000, and the most important characteristics, such as the variation of stagnation point and separation points, have been presented above.

The drag and lift forces are determined from the sum of the friction force and pressure force around the cylinder. Consider the pressure distribution around a cylinder in a shear flow, such as that in Fig. 19(b). Compared to the pressure distribution in non-shear flow, in zone A, the increased pressure on the high-velocity side and the decreased pressure on the low-velocity side cancel each other out to some extent when their contributions to drag force are considered. The increased pressure on the low-velocity side and the decreased pressure on the high-velocity side in zone B also cancel each other out. Recovery of the base pressure in the shear flow in zone C leads to a reduction in the drag coefficient. Whether the drag is increased or decreased depends on the sum of these contributions. Fig. 20 shows the variation of drag coefficient with shear parameter at all investigated Reynolds numbers along with a comparison of experimental and numerical results. Reynolds number dependence of the drag coefficient can be observed in the present simulation results. Fig. 20 shows that the increase or decrease in drag coefficient with shear parameter is so small that it seems appropriate to consider it as unchanged with shear parameter. The numerical results of Lei et al. (2000) at Re = 200 and 600 shown in Fig. 20 present a tendency for decrease in drag coefficient with increase in shear parameter. However, their simulation is two-dimensional and the drag in the non-shear condition showed significant differences from the present 3-D simulation. Nonetheless, the present simulation shows obvious differences from our experimental results (Cao et al., 2007). The difference between the turbulence intensity of the simulation and experiment is considered as the reason. The turbulence intensity increased with shear parameter from 2% to 6% in the experiment, which greatly influenced the experimental results. Adachi and Kato (1975) also remarked that their observation of the drag force

change in shear flow might be caused by the increased turbulence intensity. With respect to the pure shear effects, the present study shows a very slight influence on the drag coefficient. In addition, as shown in Fig. 20, there is an obvious change of drag coefficient around $\beta = 0.1$ for $\mathrm{Re} = 200$ and 220 due to the mode change.

However, the mean lift force (which does not occur in uniform flow) exists due to the asymmetry of the pressure distribution. Although the pressure is larger on the low-velocity side in zone B, which creates a lift force from the low-velocity side to the high-velocity side, it is larger on the high-velocity side in zone A, which creates a lift force from the high-velocity side to the low-velocity side. Fig. 21 shows that the resultant lift force acts from the high-velocity side to the low-velocity side, which means that contribution from the movement of the stagnation point is larger. An increase in lift force with direction from the high- to the low-velocity side was also reported by Sumner and Akosile (2003), Cao et al. (2007) in experimental studies, and Lei et al. (2000) in a numerical study. Tamura et al. (1980) numerically investigated the variation of drag and lift forces with shear parameter at $\mathrm{Re} = 40$ and 80. They reported that the lift force increases with shear parameter, as in the present study, but the lift force was shown to act from the low-velocity side to the high-velocity side. They explained this as the result of smaller minimum pressure at $\theta = 90^\circ$ on the high-velocity side, which creates a lift force toward the high-velocity side. The contribution of the movement of the stagnation point was not mentioned in their study.

The above results confirmed and added new information to the understanding of the flow mechanism around a circular cylinder as proposed by Cao et al. (2007). In the fore-body of a cylinder (zone A), the stagnation point moves to the high-velocity side, so the flow on the low-velocity side is more accelerated than on the high-velocity side. This leads to low pressure on the low-velocity side. Movement of the stagnation point is mainly influenced by the shear parameter, and Reynolds number has little influence in determining the movement of the stagnation point at relatively high Reynolds number. After that, in zone B, the velocity difference between the two sides dominates and results in a larger pressure on the low-velocity side. Reynolds number greatly influences the variation of the separation point. The drag and lift forces are determined by the individual distribution of two factors: velocity shear and accompanying movement of the stagnation point. However, considering the behavior around the cylinders, it can be concluded that the drag force was influenced very little, while the lift force was greatly influenced by the velocity shear, and the lift force is observed to act from the high-velocity side to the low-velocity side.

Finally, because the lift force is mainly caused by the movement of the stagnation point and the drag coefficient is almost unchanged in the shear flow, the lift force, which has important engineering significance, may be estimated very roughly as follows. Fig. 22 illustrates two coordinate systems, in which coordinate (x', y') is θ_0 degrees rotated from coordinate (x, y), where θ_0 is the degree of movement of the stagnation point. Thus, it is possible to estimate the lift coefficient from $|C_L| = C_D \times \tan(\theta_0)$. Fig. 23 compares the estimated and calculated lift coefficients at all investigated shear parameters and three Reynolds numbers $\mathrm{Re} = 150$, 500 and 1000, as an example. The lift coefficient is overestimated and the error increases with the shear parameter. The error is about 10.0% at $\beta = 0.1$ and 12.6% at $\beta = 0.3$ at $\mathrm{Re} = 1000$. Actually, this estimation method is based on the assumption that the pressure distribution in the shear flow is symmetrical with respect to the x'-axis. However, Fig. 24 shows that the pressure distribution is not really symmetric with respect to the x'-axis, and it is the main reason for the estimation error. However, this simple method for estimating the lift force is very easy to use.

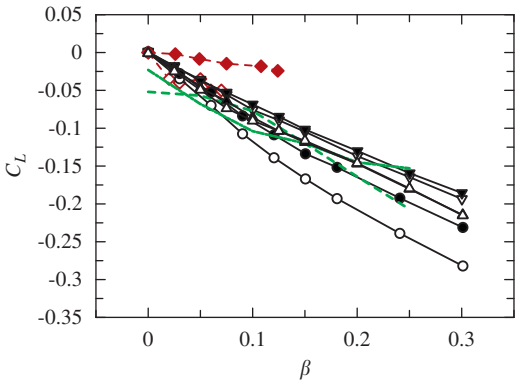

Fig. 21. Variation of lift coefficient with shear parameter at different Reynolds numbers: ○, Re = 60; ●, Re = 150; △, Re = 200; ▲, Re = 220; ▽, Re = 500; ▼, Re = 1000; ◇, Sumner and Akosile (2003); ◆, Cao et al. (2007); – –, Re = 200, Lei et al. (2000); and ····· Re = 600, Lei et al., 2000.

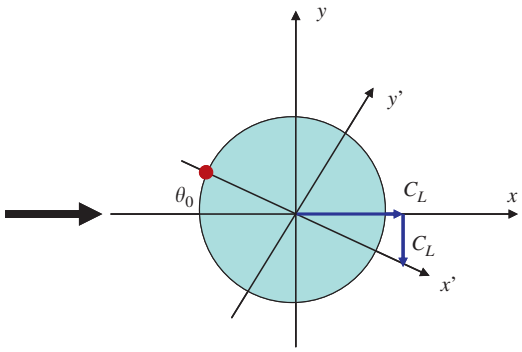

Fig. 22. Rotated coordinate to estimate lift coefficient.

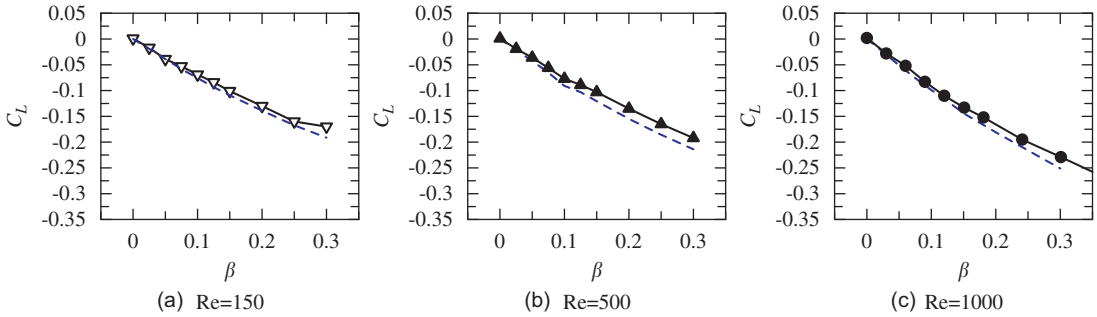

Fig. 23. Comparison of estimated and calculated lift force coefficients.

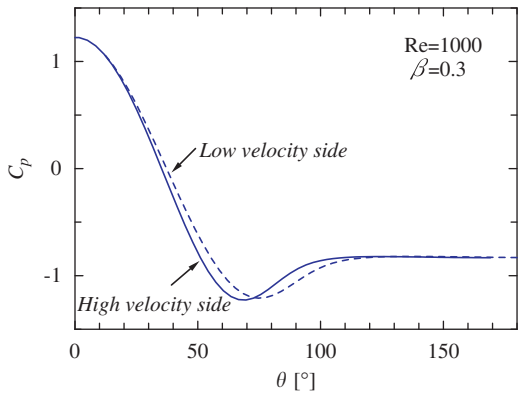

Fig. 24. Pressure distribution around cylinder with respect to rotated axis.

4. Conclusions

Three-dimensional Direct Numerical Simulation (DNS) and Large Eddy Simulation (LES) are performed to investigate the shear effects on the flow around a circular cylinder at Reynolds numbers of Re = 60–1000. Variations of Strouhal number, drag and lift coefficients and unsteady wake structures with shear parameter are studied as well as their dependences on Reynolds number.

The Strouhal number is almost unchanged in the shear parameter range of 0–0.30 at Re = 60–1000. The three-dimensionality of mode A wake instability is suppressed to two-dimensional parallel vortex shedding at Re = 200 at certain shear parameters. Karman vortex shedding was not completely suppressed in the investigated ranges of Reynolds number and shear parameter. However, the vortices on the low-velocity side disappear in the far wake in the strong shear parameter

condition. Large acceleration occurs on the low-velocity side, which self-adjusts the asymmetry in the oncoming flow in the near wake of the cylinder.

The stagnation point moves to the high-velocity side in shear flows. The movement of the angle of the stagnation point increases with shear parameter. The Reynolds number has little influence in determining the movement of the stagnation point at relatively high Reynolds number. The separation point moves downstream on the high-velocity side and upstream on the low-velocity side. The movement of the angle of the separation point increases with shear parameter. Reynolds number greatly influences the magnitude of movements of separation points.

Velocity shear and the accompanying movement of the stagnation point simultaneously influence the pressure distribution around the cylinder but with opposite contributions. In the range of $Re = 60–1000$ and $0 < \beta < 0.3$, the drag force is almost unchanged with increasing shear parameter. Lift force occurs in the shear flow due to the asymmetry of pressure distribution around the cylinder and acts from the high-velocity side to the low-velocity side. Movement of the stagnation points contributes more to the lift force than the velocity shear. Finally, a simple but very easy-to-use method is proposed to estimate the lift force in shear flow.

Acknowledgements

The authors thank the referees whose constructive comments led to an improved paper. The authors are grateful to the Ministry of Education, Culture, Sports, Science and Technology, Japan, through the Global COE Program, 2008–2012 and Chinese NSFC Funding no. 50978202.

References

Adachi, T., Kato, E., 1975. Study on the flow about a circular cylinder in shear flow. Transactions of the Japan Society for Aeronautical and Space 256, 45–53.

Cao, S., Ozono, S., Hirano, K., Tamura, Y., 2007. Vortex shedding and aerodynamic forces on a circular cylinder in linear shear flow at subcritical Reynolds number. Journal of Fluids and Structures 23, 703–714.

Cantwell, B., Coles, D., 1983. An experiment study of entrainment and transport in the turbulent near wakes of a circular cylinder. Journal of Fluid Mechanics 136, 321.

Germano, M., Piomelli, U., Moin, P., Cabot, W.H., 1991. A dynamic subgrid-scale viscosity model. Physics of Fluids, A 3 (7), 1760–1765.

Hayashi, T., Yoshino, F., 1990. On the evaluation of the aerodynamic forces acting on a circular cylinder in a uniform shear flow. Transactions of the Japan Society for Mechanical Engineering 56 (552), 31–36.

Kang, S., 2006. Uniform-shear flow over a circular cylinder at low Reynolds numbers. Journal of Fluids and Structures 22, 541–555.

Kida, S., Tanaka, M., 1994. Dynamics of vertical structures in a homogenous shear flow. Journal of Fluid Mechanics 274, 43–68.

Kim, J., Moin, P., 1985. Application of a fractional-step method to incompressible Navier–Stokes equations. Journal of Computational Physics 59, 308–323.

Kiya, M., Tamura, H., Arie, M., 1980. Vortex shedding from a circular cylinder in moderate-Reynolds-number shear flow. Journal of Fluid Mechanics 141, 721–735.

Kwon, T.S., Sung, H.J., Hyun, J.M., 1992. Experimental investigation of uniform shear flow past a circular cylinder. ASME Journal of Fluids Engineering 114, 457–460.

Kravchenko, A.G., Moin, P., 2000. Numerical studies of flow over a circular cylinder at Re = 3900. Physics of Fluids 12 (2), 403–417.

Lei, C., Cheng, L., Kavanagh, K., 2000. A finite difference solution of the shear flow over a circular cylinder. Ocean Engineering 27, 271–290.

Lilly, D.K., 1992. A proposed modification of the Germano subgrid-scale closure model. Physics of Fluids, A 4 (4), 633–635.

Lourenco, M., Shih, C., 1993. Characteristics of the plane turbulent near wake of a circular cylinder. A particle image velocimetry study, extracted from Kravchenko and Moin (2000).

Ong, L., Wallace, J., 1996. The velocity field of the turbulent very near wake of a circular cylinder. Experiments in Fluids 20, 441–453.

Persillon, H., Braza, M., 1998. Physical analysis of the transition to turbulence in the wake of a circular cylinder by three-dimensional Navier–Stokes simulation. Journal of Fluids Mechanics 365, 23–88.

Sumner, D., Akosile, O.O., 2003. On uniform planar shear flow around a circular cylinder at subcritical Reynolds number. Journal of Fluids and Structures 18, 441–454.

Tamura, H., Kiya, M., Arie, M., 1980. Numerical study of viscous shear flow past a circular cylinder. Transactions of the Japan Society for Mechanical Engineering 46 (404), 555–564.

Tamura, T., Kitagishi, T., 2001. Application of the interpolation method in generalized coordinate system to wake flows around a circular cylinder. Journal of Structural and Constructional Engineering, AIJ 545, 27–34.

Williamson, C.H.K., 1996. Vortex dynamics in the cylinder wake. Annual Review of Fluid Mechanics 28, 477–539.

Zang, Y., Street, R.L., Koseff, J.R., 1994. A non-staggered grid, fractional step method for time-dependent incompressible Navier–Stokes equations in curvilinear coordinates. Journal of Computational Physics 114, 18–33.

Zhang, H.Q., Fey, U., Noack, B.R., 1995. On the transition of the cylinder wake. Physics of Fluids 7 (4), 779–794.